

Temporally Guided Articulated Hand Pose Tracking in Surgical Videos

Nathan Louis, Luowei Zhou, Steven J. Yule, Roger D. Dias,
Milisa Manojlovich, Francis D. Pagani, Donald S. Likosky, Jason J. Corso

Abstract—Articulated hand pose tracking is an under-explored problem that carries the potential for use in an extensive number of applications, especially in the medical domain. With a robust and accurate tracking system on *in-vivo* surgical videos, the motion dynamics and movement patterns of the hands can be captured and analyzed for many rich tasks. In this work, we propose a novel hand pose estimation model, Res152-CondPose, which improves detection and tracking accuracy by incorporating a hand pose prior into its pose prediction. We show improvements over state-of-the-art methods which provide frame-wise independent predictions, by following a temporally guided approach that effectively leverages past predictions. Additionally, we collect the first dataset, *Surgical Hands*, that provides multi-instance articulated hand pose annotations for *in-vivo* videos. Our dataset contains 76 video clips from 28 publicly available surgical videos and over 8.1k annotated hand pose instances. We provide bounding boxes, articulated hand pose annotations, and tracking IDs to enable multi-instance area-based and articulated tracking. When evaluated on *Surgical Hands*, we show our method outperforms the state-of-the-art method using mean Average Precision (mAP), to measure pose estimation accuracy, and Multiple Object Tracking Accuracy (MOTA), to assess pose tracking performance. Both the code and dataset are available at https://github.com/MichiganCOG/Surgical_Hands_RELEASE.

Manuscript submitted 01/11/2021. This project was supported by the National Heart, Lung, and Blood Institute (NHLBI: R01HL146619) and the University of Michigan (U-M's Mcubed Program). Opinions expressed in this manuscript do not represent those of The NIH or the US Department of Health and Human Services or the US Department of Veterans Affairs.

N. Louis is with the Department of Electrical Engineering and Computer Science, University of Michigan, Ann Arbor, MI 48109 USA (e-mail: natlouis@umich.edu).

J. J. Corso is with the Stevens Institute for Artificial Intelligence and the Department of Computer Science at Stevens Institute of Technology, Hoboken, NJ 07030 USA (e-mail: jcorso@stevens.edu). This work was conducted while he was with the Department of Electrical Engineering and Computer Science, University of Michigan, Ann Arbor, MI 48109 USA.

L. Zhou is with Cloud and AI, Microsoft, Redmond, WA 98052 USA (e-mail: luozhou@microsoft.com).

S.J. Yule is with the Department of Clinical Surgery, University of Edinburgh, Edinburgh, SCT UK (e-mail: steven.yule@ed.ac.uk).

M. Manojlovich is with the School of Nursing, University of Michigan, Ann Arbor, MI 48109 USA (e-mail: mmanojlo@med.umich.edu).

R.G. Dias is with the Department of Emergency Medicine, Harvard Medical School, Boston, MA 02115 USA (e-mail: rdias@bwh.harvard.edu).

F.D. Pagani and D.S. Likosky are with the Department of Cardiac Surgery, University of Michigan, Ann Arbor, MI 48109 USA (e-mail: fpagani@med.umich.edu; likosky@med.umich.edu).

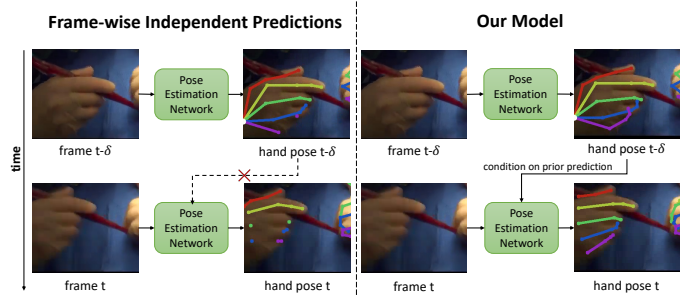


Fig. 1: We show a real example from *Surgical Hands*. On the left, a method only performing frame-wise independent predictions may miss out on properly localizing joints, while on the right, temporally passing past predictions from previous frames improves the network's localization.

Index Terms—Articulated pose, surgical videos, computer vision, hand pose, video tracking

I. INTRODUCTION

Machine learning and computer vision have become increasingly integrated with healthcare in the medical community. This is apparent in the myriad of tasks such as cancer [1] and diabetic retinopathy classification [2], tumor segmentation [3], clinical competence and technical skill assessment [4]–[8], and tool detection and tracking [9]–[12]. In this work we open avenues for new problems introduced by the use of novel automatic articulated hand pose tracking in the surgical domain. Detecting and Tracking hand poses can enable us to perform other useful tasks such as technical skill assessment, temporal action recognition, and training surgical residents. Currently these tasks may require tedious manual review from health care professionals, but by capturing and leveraging rich video features we can automate many of these processes in the future.

Articulated pose tracking in the computer vision community is primarily centered around human poses [17]–[25], while in the medical community works have focused on detection and tracking of surgical instruments [9]–[12]. Detecting and tracking surgical instruments can be useful for additional tasks, but the instruments are inherent only to the surgical procedures used during training. We seek to bring articulated hand pose tracking into the surgical domain, while abstracting away the

TABLE I: We compare our proposed dataset to other existing hand pose datasets. Our data supports multiple object instances, along with tracking, in each clip.

Name	Labels	Environment	# dets	Detection	Multi-instance	Tracking
CMU Manual Hands (MPII+NZSL) [13]	Manual	In-the-wild + Same background	2.8k	✓	✓	✗
CMU Synthetic Hands [13]	Synthetic	Renderer	14.2k	✓	✓	✗
Panoptic Hands [13]	Trained Network	Multiview-camera studio	14.8k	✓	✓	✗
LSMV 3D [14]	Leapmotion sensor	Research office	184k	✓	✗	✗
Freihand [15]	Hybrid	Green screen + Indoor/outdoor	36.5k	✓	✗	✗
STB [16]	Manual	Indoor	18k	✓	✗	✓
<i>Surgical Hands</i> (Ours)	Manual	Operating rooms	8.1k	✓	✓	✓

emphasis on surgical instruments. In our view, direct articulated hand tracking will be more widely applicable to various surgical tasks than instrument tracking. With articulated hand pose tracking, we can highlight important properties such as grip, motion, and tension that human experts often attend to when evaluating videos for technical skill, which are agnostic to the surgical instrument or procedure being carried out.

One of the challenges in pose tracking is the temporal consistency of predictions between frames, the lack of which can lead to flickering and unfeasible changes in estimated poses. Most of the works [17], [20], [21], [23]–[25] in articulated pose tracking use frame-wise independent predictions. There are works in human pose tracking that use optical flow [18] and deformable convolutions [19] to spatially transform predictions or 3d-convolutions [22] to gather temporal context, but they do not integrate past inferences when producing new predictions.

Therefore we propose **Res152-CondPose**, a new model that performs predictions conditioned on the pose estimates of prior frames. In Fig. 1, we show a comparison of both approaches: a model that uses frame-wise independent predictions and our model which uses conditional predictions. The model’s pose estimate between frames may fluctuate due to varying factors such as lighting, hand orientation, or motion blur. But we show that using prior predictions as guidance, we can improve our localization accuracy. When observing a hand in a video, the internal representation of this object’s state (position, appearance, and classification) is a function of its current state and its previous states. Therefore in tracking, it intuitively makes sense to make decisions about an object’s state using previous states as well. Our model uses a deep artificial neural network to perform articulated hand pose tracking and a recursive heatmap detection scheme to improve the localization during tracking. By learning this Markovian prior for the prediction of hand joints, we can improve both pose estimation and consequently final tracking accuracy performance.

However, to validate our idea, we lack a major benchmark on articulated hand pose tracking in the surgical domain. Active research for computer vision in the medical field predominantly use robotic-assisted surgery (RAS) [9]–[12], [26], [27] videos, with detection and tracking annotations that are instrument or procedure specific and naturally cannot extend to novel videos containing unseen instruments. Instead, we annotate the articulated hand poses of surgeons which subsumes both surgical instrument and non-instrument actions, e.g. suturing, knot-tying, and gesturing. We collect a

novel dataset named *Surgical Hands*. Our dataset consists of intraoperative videos of real surgeries featuring hand use in many instrument and non-instrument actions. From publicly available videos we extract video clips and collect articulated pose annotations that label all of the visible hands and hand joints in the scene. We are, to the best of our knowledge, the first to introduce a labeled dataset for both detection and tracking of multiple articulated hand poses. We benchmark our dataset against existing tracking baselines and demonstrate the superiority of our proposed approach on both hand pose estimation and tracking.

Our contributions in this work are as follows:

- We introduce **Res152-CondPose**, a novel deep network that takes advantage of confident prior predictions to improve localization accuracy and tracking consistency.
- We present *Surgical Hands*, a new video dataset for multi-instance articulated hand pose estimation and tracking in the *in-vivo* surgical domain.
- We set new state-of-the-art benchmark performance on *Surgical Hands*.

II. RELATED WORKS

A. Detection and Tracking in the Medical Domain

Data-driven methods in the medical video domain, predominantly consist of RAS videos. Unlike our work, RAS videos exclusively contain surgery-specific instruments. Works in this area perform subtasks such as surgical instrument detection, localization, tracking, and skill ranking [9]–[12], [26], [27]. For detection, methods [5]–[7] have traditionally used kinematic data directly which requires an external apparatus, e.g. the da Vinci Surgical System (dvSS), to capture these measurements. But full kinematic information is only available for robotic-controlled tools, even less so for hand-held instruments. Adding any external apparatus to capture kinematic data can negatively impact the costs, flexibility, and performance of certain operations.

In contrast to manually measuring kinematics, computer vision-based approaches extract information directly from video data to perform object detection. Khalid et al. [28] and Jin et al. [27] both use a vanilla region proposal network, such as FasterRCNN [29], as their base detection architecture and perform localization tasks on the resulting bounding boxes. Sarikaya et al. [9] modified FasterRCNN to use optical flow frames as an additional branch input to detect the pincers of robotic tools. Laina et al. [30] improved upon this localization for surgical instruments by simultaneously

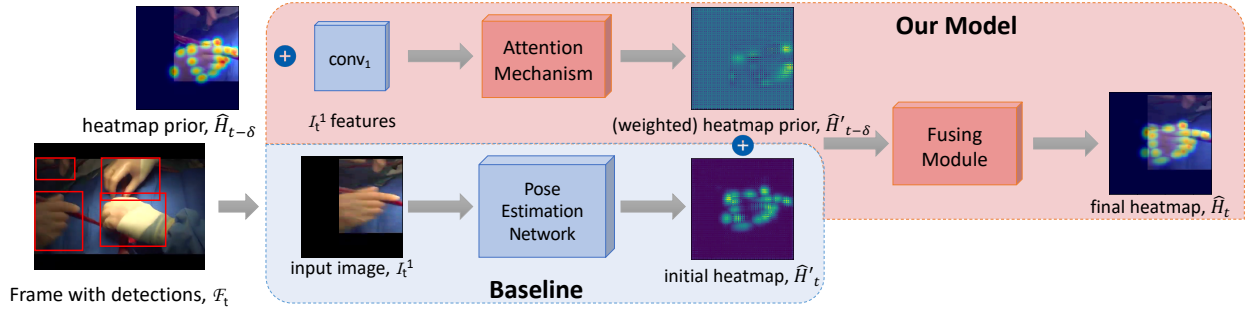


Fig. 2: From the current video frame, we crop and center every detection to the input image, I_t^n . The baseline generates a heatmap, \hat{H}'_t , for each detection using a pose estimation network [18]. In our model, we provide additional information to this heatmap by incorporating a heatmap prior from $t - \delta$. We concatenate the $conv_1$ features at t with $\hat{H}_{t-\delta}$, the predicted output of the same object at $t - \delta$. We pass this through our attention mechanism to produce a weighted heatmap prior, $\hat{H}'_{t-\delta}$, adding the context of $conv_1$ features. Both \hat{H}'_t and $\hat{H}'_{t-\delta}$ are concatenated and passed through the fusing module, using features from both heatmaps to produce the final articulated hand pose estimate.

solving a segmentation and localization task. Ni et al. [11] performed semantic segmentation on different robotic tools by introducing RASNet, a U-shaped network that included a global attention mechanism. From these RAS works, Du et al. [31] is most similar to ours. They construct the articulated pose from the detected points and joints in a bottom-up fashion, using bipartite graph matching. Conversely, we estimate the joints of hands from bounding box detections using a top-down approach and perform tracking from those detections. In a follow-up work [10] the authors use a 3D network architecture and provide more labeled annotations.

For tracking, earlier published works have learned a similarity function based on weighted mutual information [32] or a unified detection-tracking framework [33] that utilizes Bayesian filtering and treats detection and surgical instrument tracking as a minimization problem. Later, Nwoye et al. [12] introduced a weakly-supervised approach that uses coarse binary labels to indicate the presence or absence of seven surgical tools. They are the first to use the Multiple Object Tracking Accuracy (MOTA) [34] metric for surgical tool tracking for endoscopic surgery videos. However, their video data contain at most one unique type of tool at each frame; hence, it can be narrowed down to an object detection problem. Unlike their work, we support multiple tracking instances of the same object in each frame. In our work, we will be using MOTA as part of our performance metrics for tracking the hands of the surgeons in our videos. Most recently, Zhang et al. [35] presented an object detector trained on bounding box annotations of hands in operating rooms. This contrasts with our work where we provide articulated poses, integrate past predictions to improve pose estimations, and a benchmark for evaluating the quality of tracking.

B. Articulated Pose Estimation and Tracking

1) *Human Pose*: Articulated pose estimation and tracking is commonly applied to images and videos of people. Methods for this task are grouped into top-down [18]–[22] and bottom-up [23]–[25]. Top-down methods first detect and crop all persons from an image using an object detector. Then for

each crop the human pose is regressed independently using a pose estimation network. Bottom-up methods localize all joints throughout the entire image, and then use bipartite matching and graph minimization techniques to assign joints to each person. As top-down approaches typically perform best in practice, we follow this paradigm.

In our work we borrow our pose estimation model from [18] which uses a ResNet architecture followed by deconvolutional layers to produce localization heatmaps of human joints. For tracking, their method uses greedy matching and select the highest intersection-over-union (IoU) overlap from detected bounding boxes between adjacent frames. To incorporate some temporal consistency, they include bounding boxes of poses propagated from previous frames using computed optical flow. However, this approach cannot improve predicted poses it can only spatially shift them from estimated optical flow.

Bertasius et. al. [19] perform another type of pose propagation by using deformable convolutions to apply a learned transform that warps the predicted pose from the first frame onto a second frame. They are similar to our work where they use the output heatmap from both frames to generate a new output, but pose warping does not overcome missed or erroneous pose predictions between frames; our method can overcome these problems because it integrates newly inferred pose at each frame before producing the new heatmap output.

Another method for tracking by Ning et al [21] utilizes a Graph Convolutional Network (GCN) [36] to generate embeddings from detected poses to match across video frames. This introduces robustness because, in spite of large camera movements, the human pose remains stable for small time steps. Ideally, GCN tracking would succeed in cases of considerable and shaky camera movements where IoU tracking may fail due to large changes in on-screen position. One drawback is that for a relatively stable camera position and multiple similar poses, e.g. on-stage dance routine, the embedded features become very similar and increasingly difficult to separate. Hence we introduce a visual feature embedding, extracted from each image crop, in addition to the embedded pose of each hand.

2) *Hand Pose*: Existing work on 2D hand pose estimation [13], [15], [37] is analogous to human pose estimation. However, we are not aware of existing deep learning-based methods evaluated on hand pose tracking. Simon et al. [13] provide a method that helps a network improve its detection of occluded joints by training on multiple views of the same scene. Santavas et al. [37] introduced a self-attention module to their estimation network, and Zimmerman et al. [15] introduce a dataset for the 3D pose estimation from RGB image task. We introduce a new video dataset for multi-instance articulated hand pose tracking in the in-vivo surgical environment. As shown in Table I, many existing datasets support detection with no temporal coherence between video frames. The only dataset that claims tracking is STB [16]; however, their dataset consists of only a single hand throughout their video sequences and at most one detection per frame. Our data includes varying lighting conditions, fast movement, and diversity in scene appearances. Distinctively, we also include gloved hands, which appear in contrasting colors such as latex and green. To our knowledge, we are the first to provide annotated data and a substantially strong baseline to compare against for the articulated hand pose tracking task.

III. METHOD

In the articulated pose tracking domain, many prior works have used models that only generate frame-wise independent pose predictions. Even optical flow [18] or deformable convolution [19] techniques do not account for confidences of past observations, which play an important role for temporally-informed predictions. To overcome these limitations, we propose **Res152-CondPose**, which performs articulated pose detection and tracking by incorporating previous observations as prior guidance.

We show our model in Fig. 2. While the baseline simply produces a heatmap from each hand using a pose estimation network, we incorporate previous predictions into our final heatmap output. By leveraging past predictions from our model, we can produce conditioned hand pose outputs, improving detection performance during inference. **Res152-CondPose** is designed for video data, so we begin by pre-training our pose estimation network on an image dataset [13]. Then, we finetune on our video dataset, *Surgical Hands*, training our model to make conditioned hand pose predictions. Last, we introduce and experiment with a learned joint visual-pose embedding used within a graph convolutional network for tracking hand poses.

A. Hand Pose Estimation in Images

First, we begin by pretraining our pose estimation model on an image dataset [13]. Our base network is borrowed from Xiao et al. [18] and uses a ResNet backbone architecture. This an encoder-decoder style network that upsamples feature maps into a final heatmap prediction, $\hat{\mathcal{H}}$. The details of this architecture are encapsulated into the pose estimation network shown in Fig. 2.

We define the basic input and output for the pose estimation network, P , as $\hat{\mathcal{H}} = P(\mathcal{I})$. The input is an image crop \mathcal{I} ,

$\mathcal{I} \in \mathbb{R}^{H \times W \times 3}$, and the output is a predicted heatmap $\hat{\mathcal{H}}$, $\hat{\mathcal{H}} \in \mathbb{R}^{H' \times W' \times J}$. Here H, W represents the input image height and width and H', W' are the output heatmap height and widths. J represents the number of predicted joints of each hand. Each image crop is extracted from the object's bounding box, and the size is empirically chosen to be 2.2 times the total area of the object's bounding box.

We train our network using the mean squared error (MSE) loss between the ground truth heatmap, \mathcal{H} , and the predicted heatmap, $\hat{\mathcal{H}}$, shown as

$$\mathcal{L} = \|(\mathcal{H} - \hat{\mathcal{H}}) \odot \mathcal{M}\|^2. \quad (1)$$

The ground truth heatmaps, \mathcal{H} , are generated from 2D Gaussians centered on each annotated keypoint. Not all joints are visible and annotated, so a binary mask, \mathcal{M} , is included to mask out those un-annotated joints. They will not factor into the loss calculation. During evaluation, the final joint location is from the position of the maximum value for each joint prediction in $\hat{\mathcal{H}}$. After completing the pretraining, we finetune our model on videos to learn conditional hand pose predictions.

B. Hand Pose Estimation in Videos

While an image dataset, from the previous section, cannot be used to learn our conditional hand pose predictions, we can still use it to learn weights that can speed up our training process and improve generalizability. We finetune our full network, **Res152-CondPose**, on our video dataset, *Surgical Hands*, as shown in the top portion of Fig. 2. To incorporate a prior branch, we introduce a heatmap prior, $\hat{\mathcal{H}}_{t-\delta}$, a pose estimate of the same object from $t - \delta$. Our model performs conditional predictions, which we define as

$$\hat{\mathcal{H}}_t = M_{fus}(P(\mathcal{I}_t); M_{att}(v_t; \hat{\mathcal{H}}_{t-\delta})). \quad (2)$$

For each input frame, \mathcal{I}_t , we output the localization heatmap $\hat{\mathcal{H}}_t$. In contrast to our previous definition of P , this output is conditioned on the network's prediction at a previous time step $t - \delta$. Our model is further composed of two branches: the attention mechanism, M_{att} , and the fusing module, M_{fus} . P is the base pose estimation network.

The attention mechanism, M_{att} contextualizes the prior heatmap prediction, $\hat{\mathcal{H}}_{t-\delta}$, with the current image visual features, v_t . The purpose of this branch is to relate the visual representation of a hand and its localized heatmap prior, ideally learning to weight each joint prior accordingly. We use the *conv_1* feature output from the base network to represent the visual features from the image, and concatenate this with the aligned previous heatmap prediction. M_{att} is composed of two convolutional layers, followed by transposed convolution, with ReLU non-linearities in-between.

Our fusing module, M_{fus} , has an identical architecture to M_{att} . However, this is trained to produce the final heatmap output from the concatenation of our initial prediction, $\hat{\mathcal{H}}'_t$, and our heatmap prior, $\hat{\mathcal{H}}'_{t-\delta}$. This branch produces a merged final heatmap, $\hat{\mathcal{H}}_t$, using the Gaussian peak magnitudes and locations from both intermediate heatmaps. For example, if the prediction at t_1 correctly localizes a joint but it misses

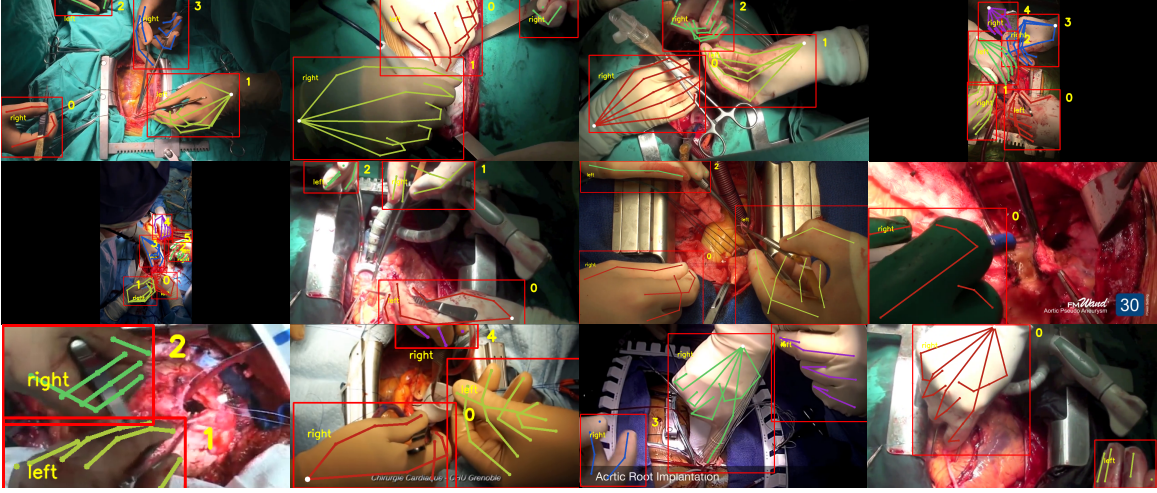


Fig. 3: Samples from crowd-sourced annotations. For each hand we provide a bounding box, a left/right hand class label, tracking id, and keypoint annotations for visible and occluded joints.

that same joint at t_2 , we expect the final output to be adjusted based on the confidences of each detection.

During training the prior is selected from frame $t - \delta$. If the object does not exist at that frame, we use earlier frames up until the first. If a corresponding object does not exist on any previous frames, then the prior, $\hat{\mathcal{H}}_{t-\delta}$, is set as a zeros heatmap. A zeros heatmap as a prior will be expected during evaluation, because priors do not yet exist at the start of a video. Also during evaluation, unlike training, the prior associated with the current detected hand is unknown. We are given n priors from time $t - 1$, $\{\hat{\mathcal{H}}_{t-1}^1, \hat{\mathcal{H}}_{t-1}^2, \dots, \hat{\mathcal{H}}_{t-1}^n\}$, and k detections (image crops) at time t , $\{\hat{\mathcal{I}}_{t-1}^1, \hat{\mathcal{I}}_{t-1}^2, \dots, \hat{\mathcal{I}}_{t-1}^k\}$. All prior and detection pairs are passed through the network to get the predicted heatmaps. But only the heatmap with the highest average confidence score (Gaussian peak) is selected as the output for that detection.

C. Matching Strategies for Tracking

After estimating the pose of the hands from each detection, we require a matching strategy to performing tracking. Given n hands at time $t - 1$, $\{o_{t-1}^1, o_{t-1}^2, \dots, o_{t-1}^n\}$, and m hands at time t , $\{o_t^1, o_t^2, \dots, o_t^m\}$, we first use a similarity function to derive similarity measures between each pair at $t - 1$ and t . Common methods are intersection-over-union (IoU) of the bounding boxes, average L2-distance of the predicted joint locations, or L2-distance between the graph pose embeddings. Here, we experiment with a modification to the graph pose embeddings that includes a visual representation of the object into the encoding.

Using IoU to match detections between time steps and perform tracking is typically the highest performing option. Operating strictly on bounding boxes of the entire hand, this strategy has the advantage of being most robust to pose prediction errors. However, the most common sources of failure from IoU are in cases of multiple overlapping objects or substantial movement. Ning et al. [21] generate a graph pose embedding from the keypoint positions of each detected person

and use it to assign human poses between frames. However, we try concatenating the embedded pose again with the *conv_1* output from the base network to encode visual information into this embedding as well. We hypothesize that this visual-pose feature embedding can disambiguate between hand poses with similar pose configurations.

Similar to Ning et al. [21] we train a GCN to output the embedding of each input hand pose, \mathcal{X} , defined simply as $\hat{p} = GCN(\mathcal{X})$. Here $\mathcal{X} \in \mathbb{R}^{J \times C}$, where J is the number of joints and C is the number of channels. We follow this with a joint-embedding layer, \mathcal{J} , that outputs a visual-pose embedding from the concatenation of the visual features, v , and the pose embedding \hat{p} , defined as $\hat{p}_v = \mathcal{J}(v; \hat{p})$. Our joint-embedding layer, \mathcal{J} consists of two fully-connected layers separated by a ReLU function. For training, we use the contrastive loss [38] defined as

$$\mathcal{L} = \frac{1}{2} (y * d + (1 - y) * \max(0, (m - d)^2)). \quad (3)$$

The contrastive loss is used to place embeddings close in perceptual distance. Meaning, visually similar pairs will be close together and dissimilar pairs will be further away. For a pair of embeddings \hat{p}_v^1 and \hat{p}_v^2 , the variable d represents the L2-distance between the two where $d = \|\hat{p}_v^1 - \hat{p}_v^2\|^2$. y is a binary label that indicates whether the two embeddings represent the same hand, 1, or different hands, 0. m is the margin variable, a hyperparameter used for tuning.

For each item in our minibatch, positive pairs are selected between adjacent frames with probability $p = 0.5$ and negative pairs are selected from the same video with $p = 0.4$ or from a different video with $p = 0.1$. We evaluate our trained GCN models using the classification accuracy between pairs of selected hands. We compare both the pose embedding and the visual-pose embedding in Sec. V. From our experiments, the GCN and GCN-joint visual models achieve classification accuracies of $> 97\%$ using features across the models.

IV. DATASET

To benchmark our method, we require data to train and evaluate our models and baselines. To that end, we introduce *Surgical Hands*, a novel video dataset for multi-instance articulated hand pose estimation and tracking in the surgical domain. We are the first to publish a labeled dataset for both detection and articulated hand pose tracking of multiple hands for videos. From publicly available videos, we selected 28 that had a view of the patient cavity and hands of the surgical team members during the operation. We then extracted 76 clips sampled at 8 frames per second and provided bounding box, class label, tracking id, and pose annotations for all hands in the scenes. We show samples of our annotations in Fig. 3.

A. Hand Pose Annotations

We used Amazon Mechanical Turk (AMT) to collect hand pose annotations and a modified version of Visipedia Annotation Tools¹ to generate bounding box annotations, class labels, and joint positions. Each hand is labeled as left or right, and consists of 21 joint annotations in total, consistent with prior works [13]. A canonical skeleton from our annotations is shown in Fig. 4. Annotators are tasked with drawing bounding boxes around each visible hand in the frame, even partially occluded hands, and labeling the joints on each hand. The joints are labeled with a keypoint that holds three properties: visible, occluded, not-available. Visible implies that the joint is visibly on screen, occluded means the joint is obstructed but its position can be estimated, not-available means the joint position cannot be inferred or it is off-screen. In addition to the bounding boxes and the labeled keypoints, unique tracking IDs were manually assigned for all hands in the video clips.

B. Dataset Statistics

From our collected data, we have 2,838 annotated frames from the 76 total clips, 8,178 unique hand annotations and a total of 21 unique annotators. Each annotated frame contains a mean of 2.88 hands, median of 3 hands, and a maximum of 7 hands. Fig. 5 shows the joint annotation visibility across our labeled frames. We see that across all instances, the joints from the ring and pinky finger show the highest rate of being visually obscured or not-available. In the majority of our video clips, position and orientation of the hand makes it extremely difficult to localize those joints. This is expected because the 4th and 5th digits are underutilized in many procedures, the first 3 digits are typically used to hold surgical instruments.

V. EXPERIMENTS AND EVALUATION

A. Implementation Details

We begin by training the pose estimation model on an image dataset for hand pose estimation, we use the CMU Manual Hands + Synthetic Hands (Mixed Hands) [13] image dataset. We start with an ImageNet pretrained ResNet-152 network architecture and using a batch size of 16 we train for 30 epochs. We use an Adam optimizer and an initial learning rate

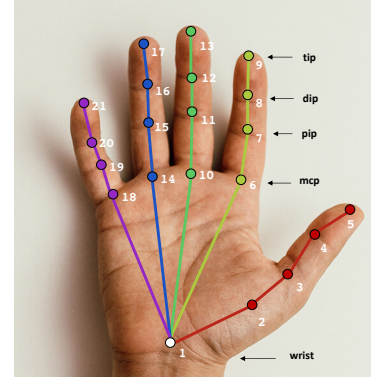


Fig. 4: There are 21 keypoints annotated for each hand. Following previous conventions [13], in addition to the wrist, we annotate the distal (dip), proximal (pip), metacarpophalangeal (mcp) joints, and the tip of each finger.

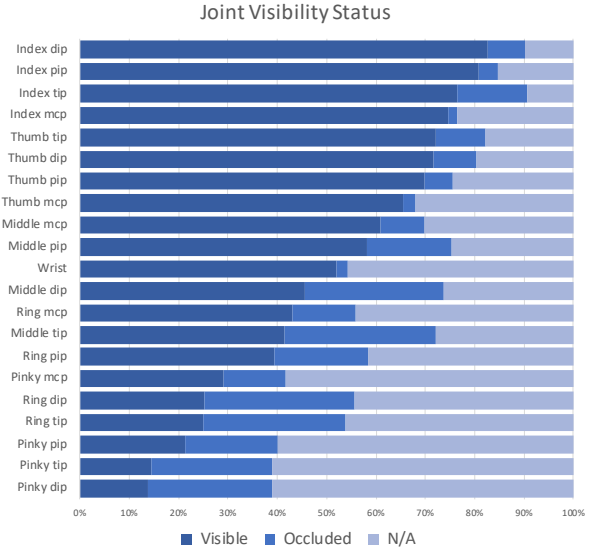


Fig. 5: Statistics on visibility of each joint. The least visible joints belong to the 4th and 5th digits, but this is expected as they are underutilized in most surgical actions.

of $1e^{-3}$, along with a linear scheduler and decay the learning rate by a factor of 10 at epoch 20. For data augmentation, following prior work, we uniformly sample a random rotation between $[-40, 40]$ degrees and a random horizontal flip of the image crop.

Next, we finetune on our *Surgical Hands* video dataset. From our 76 clips, we use leave-one-out cross-validation and split our data into 28 different folds. Clips belonging to the same video are in the same validation fold, and the computed metrics are averaged across all folds. Here we use a batch size of 12 and train for 20 epochs and an initial learning rate of $8e^{-5}$. The linear scheduler decays the learning rate at epoch 5 by a factor of 10. When training with our model, both the current image crop and prior have the same rotation and flip augmentation. For selecting the image prior, we empirically select $\delta = 3$. During training, we employ a variant of curriculum learning that gradually transitions to predicted

¹https://github.com/visipedia/annotation_tools

priors from ground truth priors. A predicted prior at $t - \delta$ is sampled with a probability of $p = 0.10 * epoch$, until only predictions are used for training at epoch 10 and onward.

Afterwards, we train our GCN and joint-embedding layer using a batch size of 32 and train for 60 epochs and an initial learning rate of $1e^{-3}$. Here our linear scheduler decays the learning rate at epochs 20 and 30 by factors of 10. To preprocess the input keypoints, \mathcal{X} , we first normalize them to be between 0-1 relative to its position along the bounding box (i.e subtract top-left (x, y) from each joint coordinate and divide by $(width, height)$, respectively). The input to the GCN follows the same convention as prior work, the dimension for each input is $J \times C$ where J represents the number of joints and C represents the number of channels. In our experiments, $C = 2$ for x-y coordinates only and $C = 3$ to include the annotation state of each keypoint (0 = unannotated or 1 = annotated). With $C = 2$, unannotated keypoints are given a default value of -1 .

B. Detection Performance

To evaluate detection performance on our *Surgical Hands* dataset, we use the mean Average Precision (mAP) metric. mAP is also the selected metric for the PoseTrack [17] metrics in the human pose tracking domain, so we adopt this as well. The mAP is computed using the Probability of Correct Keypoints (PCK) metric. The PCK metric measures the probability of correctly localizing keypoints within a given normalized threshold distance, σ , shown as:

$$P_{\sigma}^p(d_0) = \frac{1}{|\mathcal{T}|} \sum_{\tau} \delta(\|x_p - y_p\|_2 < \sigma) \quad (4)$$

We modify the PoseTrack off-line evaluation code to be compatible with our hand pose data and the distance is normalized to 0.2 times the bounding box size. 0.2 was empirically chosen to be roughly the ratio between the length of a thumb joint and the enclosing bounding box. σ is unchanged from existing code and remains 0.5. Pose predictions are assigned to ground truth poses based on the highest PCK and unassigned predictions are counted as false positives. AP for each joint is computed and mAP is reported across the entire dataset.

In all of our experiments we use leave-one-out cross validation, with 28 cross validation folds in total. Each fold contains video clips with the same source video. The presented results are the average performance across all 28 validation folds. In Table II we show the mAP at the highest Multiple Object Tracking Accuracy (MOTA) score (defined in the next section) for each model. We see that with our recursive heatmap strategy we are able to obtain higher average precision across the different joints in the hand. In Fig. 7 we show qualitative examples of our hand pose estimation on various frames from our *Surgical Hands* dataset. The top row clips are sampled from the best performing clips, while the bottom row are from the worst performing clips based on MOTA score. We see that the model suffers most in cases of heavy occlusion, where the camera view excludes the majority of the hand. Ambiguity in the position of the hand furthers the localization errors, e.g. top-down view with most fingers occluded. The

TABLE II: Mean Average Precision (mAP). Performance is averaged across all folds

Model	Wrist	Thumb	Index	Middle	Ring	Pinky	mAP
Baseline [18]	67.23	60.12	63.29	53.77	48.29	39.28	53.59
Our model	65.51	62.66	64.99	57.88	51.40	44.26	56.66

best performing cases are those with balanced lighting and an unambiguous view of the first few digits.

C. Tracking Performance

In the previous section, we measured detection which emphasizes only localization accuracy across all frames. Tracking performances also takes into account consistency of the localized keypoints across the video. To measure tracking performance, we use Multiple Object Tracking Accuracy (MOTA) scores. The MOTA metric is part of the CLEAR MOT metrics [34] and is also included in the PoseTrack metrics. It is defined as:

$$MOTA = 1 - \frac{\sum_t (FN_t + FP_t + IDSW_t)}{\sum_t G_t} \quad (5)$$

This encapsulates many errors that may occur during multiple object tracking: false negatives (FN), false positives (FP), and identity switches ($IDSW$). FN are joints for which no hypothesis/prediction was given, FP are all the hypothesis for which no real joints exists, and $IDSW$ are all occurrences in which the tracking id for two joints are swapped. G represents the total number of ground truth joints. The range of values for the $MOTA$ score is $(-\infty \text{ to } 100]$.

The four methods we experiment with are: IoU overlap, L2-distance, GCN, and GCN-joint visual. IoU overlap is the most common method, also known as spatial consistency. It involves measuring the overlap between the bounding boxes at the previous frame and the current frame. The detections with the highest overlap is selected as the same object. L2-distance is measured as the average L2 distance of the regressed keypoints between detections at time $t - 1$ and t . GCN measures the embedding similarity between the encoded keypoints at different time steps, the embeddings closest in distance are selected as matches. We experiment with GCN-joint visual which also measures embedding distance, except we use our pose-visual embeddings from each object.

We show quantitative results from our experiments in Table IV and the per-joint performance in Table III. Each row is maximized for the highest MOTA score across all hyperparameters, shown along with its corresponding mAP. We found GCN-joint visual to perform slightly better than GCN on our model, but still lower than IoU and L2. We do not include it as a comparison in our final table but leave it in the Appendix. Our method has a marginally higher MOTA score across all of the videos, but our corresponding mAP scores are greater by a much larger margin. This points to our advantage from temporally leveraging predictions from previous frames during the detection step. We show an example from a clip in Fig. 6, in a frame-by-frame comparison between the baseline and our method, we note a higher recall and improved localization. In this case the last digit is obstructed, but its position can be

TABLE III: We optimize for the Multiple Object Tracking Accuracy (MOTA), each performance metric is averaged across all validation folds

Model	MOTA Wrist	MOTA Thumb	MOTA Index	MOTA Middle	MOTA Ring	MOTA Pinky	MOTA Total	MOTP Total	Prec. Total	Rec. Total	F ₁ Score Total
Baseline [18]	36.7	45.83	57.35	45.53	34.63	8.49	38.27	85	78.3	59.13	67.37
Our Model	30.99	44.74	58.21	48.90	36.46	10.39	39.31	85.28	77.61	62.69	69.35

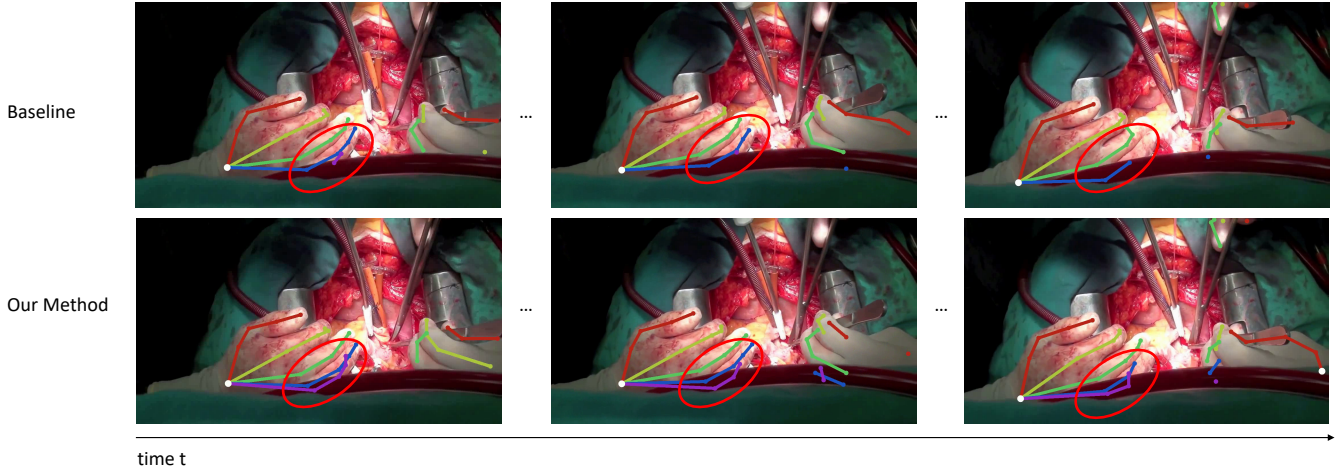


Fig. 6: We show a qualitative comparison between the baseline model and our method. We note a higher recall and consistency between frames, as shown for the hand to the left. Even when the pinky finger is not visible, the past predictions helps reinforce those joint locations.

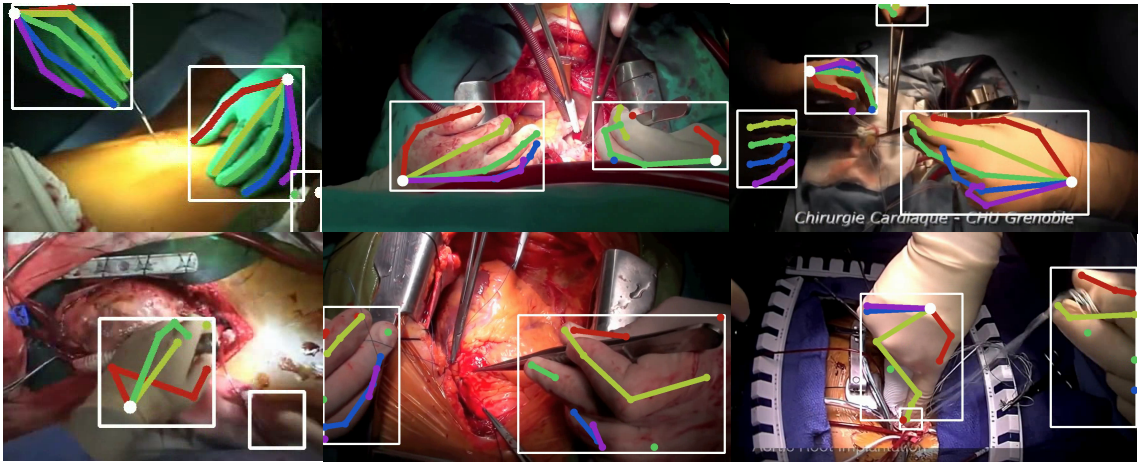


Fig. 7: (Best viewed in color). These qualitative examples are generated using bounding boxes from an object detector. We sample frames from the best performing folds (top row) and lower performing folds (bottom row). Each digit is colored differently to assess the prediction quality and accuracy.

reasonably inferred. From our annotations, this is labeled as occluded. Both methods make some prediction about this digit initially, but our model can use past predictions to reinforce its confidence while the per frame prediction may be noisy.

In top-down methods, the performance of tracking is heavily dependent on the accuracy of bounding box detections. Our earlier experiments evaluated the cross-validation splits independent of an object detector, using the ground truth annotations for the image crops. Here we use hand object

detections as input to the tracking pipeline. We use a Faster-RCNN detection architecture trained on the 100 Days of Hands (100DOH) dataset provided by Shan et al. [39]. The results are shown in the last column of Table IV. As expected, the localization and tracking accuracy are lower than when using the manually annotated bounding boxes as input. However, the trends from both experiments remain consistent. The quality of the detected bounding boxes serve as a bottleneck to the performance of the entire system. We sample clips from the

TABLE IV: MOTA performance between matching strategies, averaged across all folds. Each row is optimized for highest MOTA performance. Matching strategies share the same base model, so it is possible for them to share the same mAP score.

Model	Matching Strategy	Perfect Det.		Object Det.	
		mAP	MOTA	mAP	MOTA
Baseline [18]	IoU	53.59	38.27	48.15	31.46
	L2	52.65	37.78	47.44	31.14
	GCN	52.65	36.78	47.44	30.03
Our Model	IoU	56.66	39.31	50.04	33.19
	L2	56.66	38.94	50.04	32.84
	GCN	56.66	38.22	50.04	32.24

best and worst performing in Fig. 7.

D. Ablation Analysis

To evaluate the efficacy of each part of our model, we perform an ablative analysis on the convolutional feature map and the attention mechanism. We experiment with three different modifications to our network: no prior convolutional feature map, no attention mechanism, and removal of both. We show the results of these experiments in Table V.

As expected, the full model has the highest scores overall but the model variants are less straight forward. The addition of the attention mechanism and convolutional feature map seem to have opposing effects on the mAP and MOTA scores, respectively. The NC model does not use a convolutional feature map from frame t to gather context, so the fusing module is applied directly to both the un-modified heatmaps from $t - \delta$ and t . We found that this increases the mAP value, but lowers the MOTA score. For the NA model, we directly concatenate the convolutional features and the heatmaps, with no attention mechanism. We see that this has the opposite effect, decreasing the mAP significantly but slightly increasing the overall MOTA score. When directly using the prior without the convolutional features for context (NC and NC-NA models), we hypothesize that the model can still learn to use the prior prediction and improve its detection (mAP) score. And even more so with the attention mechanism, where it can still weigh certain joints that are more likely to improve pose prediction. Here the NA model brings a drop in mAP, which may be attributed to an unrefined prior with noisy features. Strangely, the NA model shows a small increase in the MOTA score. The MOTA metric counts tracking errors produced by the model which in our experiments were shown to be heavily-weighted by false positives. Given the lower mAP score by the NA model and the smaller margin in the MOTA metric, it is likely that the small improvement comes from fewer false positives produced by that model.

We also explored the value of our hyperparameter, δ , during training. The prior is selected from frame $t - \delta$, the higher δ lends itself to a longer temporal range. We train with values $\delta = \{1, 2, 3, 4\}$ and show our results in Table VI. In our experiments, we are optimizing for the highest MOTA score and we found that to be $\delta = 3$ with 39.31. The second highest is $\delta = 1$ with a slightly smaller MOTA score (39.03),

TABLE V: Ablation analysis using IoU matching strategy ($\delta = 1$). NC = No convolutional feature map, NA = No attention mechanism.

Model Variant	Matching Strategy	Perfect Det.	
		mAP	MOTA
NC-NA	IoU	55.23	38.31
NC	IoU	56.00	38.13
NA	IoU	54.70	38.45
Full model	IoU	58.64	39.03

TABLE VI: Effect of δ . Each model is trained with a separate δ value

Model Variant	Matching Strategy	Perfect Det.	
		mAP	MOTA
$\delta = 1$	IoU	58.64	39.03
$\delta = 2$	IoU	54.71	38.42
$\delta = 3$	IoU	56.66	39.31
$\delta = 4$	IoU	56.35	38.09

but a much higher mAP (58.64 vs 56.66). It is important to note that in our experiments hyperparameters are tuned to maximize the MOTA performance only. We also find a non-linear correlation between the mAP and MOTA scores, there is often a trade-off in mAP when optimizing for the tracking performance. Therefore the best strategy is one that maximizes MOTA accuracy with minimal loss in localization precision.

E. Evaluation on Human Pose

We executed additional experiments on the PoseTrack18 dataset between our model and the baseline. The baseline model, in the author's work, also includes optical flow during tracking evaluation. The optical flow is used only to shift the detected bounding boxes, it is not incorporated into the pose estimation model itself. Hence we use our re-implementation and add the same tracking to both. We repeat this for our dataset in the Appendix.

In Fig. 8, we show a narrowed gap in performance but our findings are consistent with our earlier experiments. We perform a grid search on hyperparameters and optimize for maximum MOTA. For the top scoring models, we have similar or higher mAP on equivalent MOTA values. Given the trade-off that occurs between mAP and MOTA, this means our model is more likely to retain its localization precision at higher tracking accuracies.

VI. DISCUSSION

In this work, we have introduced *Surgical Hands*, the first articulated multi-hand pose tracking dataset to be used in evaluating hand tracking methods. We collected data specifically to be used in the medical domain from publicly available videos of real surgical procedures. Additionally we introduced **Res152-CondPose**, a novel network that makes conditional hand pose predictions by incorporating past observations as priors. We show that when compared with a frame-wise

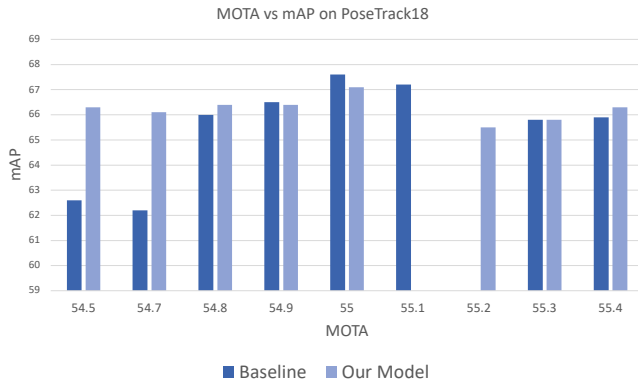


Fig. 8: Optimized for maximum MOTA score, we show the top performing models on PoseTrack18. Consistent with our earlier findings, our model has a higher mAP for comparable MOTA scores. We use our re-implementation of the optical flow track to include in the matching strategy.

independent strategy, we have better performance in detecting and tracking hand poses. Moreover, we see that our model has a much greater impact on the localization accuracy. When capturing the hand pose in videos, tracking drives the consistency of the object and joints through time. But the actual shape and characteristics of the hand is described by the localization precision. With a higher localization precision and better tracking still, we can guarantee a better representation of the hands in the scene.

While not the focus of this work, tracking hands can lead to other useful applications in the surgical domain such as technical skill assessment or temporal action detection.

With a reliable hand tracking method, we can provide a salient signal that can be used to approximate skill or understand actions.

REFERENCES

- [1] Q. Song, L. Zhao, X. Luo, and X. Dou, "Using deep learning for classification of lung nodules on computed tomography images," *Journal of healthcare engineering*, vol. 2017, 2017.
- [2] R. Casanova, S. Saldana, E. Y. Chew, R. P. Danis, C. M. Greven, and W. T. Ambrosius, "Application of random forests methods to diabetic retinopathy classification analyses," *PLOS one*, vol. 9, no. 6, p. e98587, 2014.
- [3] M. Malathi and P. Sinthia, "Brain tumour segmentation using convolutional neural network with tensor flow," *Asian Pacific journal of cancer prevention: APJCP*, vol. 20, no. 7, p. 2095, 2019.
- [4] R. D. Dias, A. Gupta, and S. J. Yule, "Using machine learning to assess physician competence: a systematic review," *Academic Medicine*, vol. 94, no. 3, pp. 427–439, 2019.
- [5] L. Tao, E. Elhamifar, S. Khudanpur, G. D. Hager, and R. Vidal, "Sparse hidden markov models for surgical gesture classification and skill evaluation," in *International conference on information processing in computer-assisted interventions*, pp. 167–177, Springer, 2012.
- [6] L. Zappella, B. Béjar, G. Hager, and R. Vidal, "Surgical gesture classification from video and kinematic data," *Medical image analysis*, vol. 17, no. 7, pp. 732–745, 2013.
- [7] G. Forestier, F. Petitjean, P. Senin, F. Despinoy, A. Hualmél, H. I. Fawaz, J. Weber, L. Idoumghar, P.-A. Muller, and P. Jannin, "Surgical motion analysis using discriminative interpretable patterns," *Artificial intelligence in medicine*, vol. 91, pp. 3–11, 2018.
- [8] S. Kumar, N. Ahmadi, G. Hager, P. Singhal, J. Corso, and V. Kroví, "Surgical performance assessment," *Mechanical Engineering*, vol. 137, no. 09, pp. S7–S10, 2015.
- [9] D. Sarikaya, J. J. Corso, and K. A. Guru, "Detection and localization of robotic tools in robot-assisted surgery videos using deep neural networks for region proposal and detection," *IEEE transactions on medical imaging*, vol. 36, no. 7, pp. 1542–1549, 2017.
- [10] E. Colleoni, S. Moccia, X. Du, E. De Momi, and D. Stoyanov, "Deep learning based robotic tool detection and articulation estimation with spatio-temporal layers," *IEEE Robotics and Automation Letters*, vol. 4, no. 3, pp. 2714–2721, 2019.
- [11] Z.-L. Ni, G.-B. Bian, X.-L. Xie, Z.-G. Hou, X.-H. Zhou, and Y.-J. Zhou, "Rasnet: Segmentation for tracking surgical instruments in surgical videos using refined attention segmentation network," in *2019 41st Annual International Conference of the IEEE Engineering in Medicine and Biology Society (EMBC)*, pp. 5735–5738, IEEE, 2019.
- [12] C. I. Nwoye, D. Mutter, J. Marescaux, and N. Padoy, "Weakly supervised convolutional lstm approach for tool tracking in laparoscopic videos," *International journal of computer assisted radiology and surgery*, vol. 14, no. 6, pp. 1059–1067, 2019.
- [13] T. Simon, H. Joo, I. Matthews, and Y. Sheikh, "Hand keypoint detection in single images using multiview bootstrapping," in *Proceedings of the IEEE conference on Computer Vision and Pattern Recognition*, pp. 1145–1153, 2017.
- [14] F. Gomez-Donoso, S. Orts-Escolano, and M. Cazorla, "Large-scale multiview 3d hand pose dataset," *Image and Vision Computing*, vol. 81, pp. 25–33, 2019.
- [15] C. Zimmermann, D. Ceylan, J. Yang, B. Russell, M. Argus, and T. Brox, "Freihand: A dataset for markerless capture of hand pose and shape from single rgb images," in *Proceedings of the IEEE International Conference on Computer Vision*, pp. 813–822, 2019.
- [16] J. Zhang, J. Jiao, M. Chen, L. Qu, X. Xu, and Q. Yang, "3d hand pose tracking and estimation using stereo matching," *arXiv preprint arXiv:1610.07214*, 2016.
- [17] M. Andriluka, U. Iqbal, E. Insafutdinov, L. Pishchulin, A. Milan, J. Gall, and B. Schiele, "Posetrack: A benchmark for human pose estimation and tracking," in *Proceedings of the IEEE Conference on Computer Vision and Pattern Recognition*, pp. 5167–5176, 2018.
- [18] B. Xiao, H. Wu, and Y. Wei, "Simple baselines for human pose estimation and tracking," in *Proceedings of the European conference on computer vision (ECCV)*, pp. 466–481, 2018.
- [19] G. Bertasius, C. Feichtenhofer, D. Tran, J. Shi, and L. Torresani, "Learning temporal pose estimation from sparsely-labeled videos," in *Advances in Neural Information Processing Systems*, pp. 3027–3038, 2019.
- [20] K. Sun, B. Xiao, D. Liu, and J. Wang, "Deep high-resolution representation learning for human pose estimation," in *Proceedings of the IEEE conference on computer vision and pattern recognition*, pp. 5693–5703, 2019.
- [21] G. Ning, J. Pei, and H. Huang, "Lighttrack: A generic framework for online top-down human pose tracking," in *Proceedings of the IEEE/CVF Conference on Computer Vision and Pattern Recognition Workshops*, pp. 1034–1035, 2020.
- [22] M. Wang, J. Tighe, and D. Modolo, "Combining detection and tracking for human pose estimation in videos," in *Proceedings of the IEEE/CVF Conference on Computer Vision and Pattern Recognition*, pp. 11088–11096, 2020.
- [23] Z. Cao, T. Simon, S.-E. Wei, and Y. Sheikh, "Realtime multi-person 2d pose estimation using part affinity fields," in *Proceedings of the IEEE conference on computer vision and pattern recognition*, pp. 7291–7299, 2017.
- [24] Y. Raaj, H. Idrees, G. Hidalgo, and Y. Sheikh, "Efficient online multi-person 2d pose tracking with recurrent spatio-temporal affinity fields," in *Proceedings of the IEEE Conference on Computer Vision and Pattern Recognition*, pp. 4620–4628, 2019.
- [25] S. Jin, W. Liu, W. Ouyang, and C. Qian, "Multi-person articulated tracking with spatial and temporal embeddings," in *Proceedings of the IEEE Conference on Computer Vision and Pattern Recognition*, pp. 5664–5673, 2019.
- [26] Y. Gao, S. S. Vedula, C. E. Reiley, N. Ahmadi, B. Varadarajan, H. C. Lin, L. Tao, L. Zappella, B. Béjar, D. D. Yuh, et al., "Jhu-isi gesture and skill assessment working set (jigsaws): A surgical activity dataset for human motion modeling," in *Miccai workshop: M2cai*, vol. 3, p. 3, 2014.
- [27] A. Jin, S. Yeung, J. Jopling, J. Krause, D. Azagury, A. Milstein, and L. Fei-Fei, "Tool detection and operative skill assessment in surgical videos using region-based convolutional neural networks," in *2018 IEEE Winter Conference on Applications of Computer Vision (WACV)*, pp. 691–699, IEEE, 2018.

- [28] S. Khalid, M. Goldenberg, T. Grantcharov, B. Taati, and F. Rudzicz, "Evaluation of deep learning models for identifying surgical actions and measuring performance," *JAMA Network Open*, vol. 3, no. 3, pp. e201664–e201664, 2020.
- [29] S. Ren, K. He, R. Girshick, and J. Sun, "Faster r-cnn: Towards real-time object detection with region proposal networks," in *Advances in neural information processing systems*, pp. 91–99, 2015.
- [30] I. Laina, N. Rieke, C. Rupprecht, J. P. Vizcaíno, A. Eslami, F. Tombari, and N. Navab, "Concurrent segmentation and localization for tracking of surgical instruments," in *International conference on medical image computing and computer-assisted intervention*, pp. 664–672, Springer, 2017.
- [31] X. Du, T. Kurmann, P.-L. Chang, M. Allan, S. Ourselin, R. Sznitman, J. D. Kelly, and D. Stoyanov, "Articulated multi-instrument 2-d pose estimation using fully convolutional networks," *IEEE transactions on medical imaging*, vol. 37, no. 5, pp. 1276–1287, 2018.
- [32] R. Richa, M. Balicki, E. Meisner, R. Sznitman, R. Taylor, and G. Hager, "Visual tracking of surgical tools for proximity detection in retinal surgery," in *International Conference on Information Processing in Computer-Assisted Interventions*, pp. 55–66, Springer, 2011.
- [33] R. Sznitman, R. Richa, R. H. Taylor, B. Jedynak, and G. D. Hager, "Unified detection and tracking of instruments during retinal microsurgery," *IEEE transactions on pattern analysis and machine intelligence*, vol. 35, no. 5, pp. 1263–1273, 2012.
- [34] K. Bernardin and R. Stiefelhagen, "Evaluating multiple object tracking performance: the clear mot metrics," *EURASIP Journal on Image and Video Processing*, vol. 2008, pp. 1–10, 2008.
- [35] M. Zhang, X. Cheng, D. Copeland, A. Desai, M. Y. Guan, G. A. Brat, and S. Yeung, "Using computer vision to automate hand detection and tracking of surgeon movements in videos of open surgery," *arXiv preprint arXiv:2012.06948*, 2020.
- [36] S. Yan, Y. Xiong, and D. Lin, "Spatial temporal graph convolutional networks for skeleton-based action recognition," in *Thirty-second AAAI conference on artificial intelligence*, 2018.
- [37] N. Santavas, I. Kansizoglou, L. Bampis, E. Karakasis, and A. Gasteratos, "Attention! a lightweight 2d hand pose estimation approach," *arXiv preprint arXiv:2001.08047*, 2020.
- [38] R. Hadsell, S. Chopra, and Y. LeCun, "Dimensionality reduction by learning an invariant mapping," in *2006 IEEE Computer Society Conference on Computer Vision and Pattern Recognition (CVPR'06)*, vol. 2, pp. 1735–1742, IEEE, 2006.
- [39] D. Shan, J. Geng, M. Shu, and D. F. Fouhey, "Understanding human hands in contact at internet scale," in *Proceedings of the IEEE/CVF Conference on Computer Vision and Pattern Recognition*, pp. 9869–9878, 2020.

Appendix

I. INFERENCE ON A VIDEO

During training, all priors from the dataset are known at time $t - \delta$. But, as mentioned in Sec. III-B, we do not have the correspondence between each prior and current image crop during validation or testing. So we filter out improbable priors using two steps:

- 1) Reprojection of predictions back onto the full frame
- 2) Thresholding the average peak Gaussian across joint predictions

When we reproject the spatial position of the prediction back onto the full frame, the relevant cropped region gives us an easy way of deducing whether this is for the same object. For extremely large displacement, the prior will have values of all zero and hence can be tossed as a potential prior for the current object. We also use a minimum Gaussian peak threshold hyperparameter, where we average the peak prediction values for each joint. This removes the lower confident predictions that may not serve to improve the current prediction. In practice, we found this value to be between 0.20-0.25 for our best performing models, on a scale from 0 to 1.0. This means, to maximize performance, the average prior peaks must be at least that high.

We show how our model functions during inference in Fig. 1. Time step t has only one prior and detected hand, so this pair is used to perform a prediction at time t . At time $t + 1$, a new object is introduced hence its prior is just a heatmap of zero values. And at time $t + 2$, we use each appropriate prior with its image crop reducing the number of priors by referencing our filtering steps again.

II. MODEL ARCHITECTURE AND TRAINING DETAILS

We show some additional details of each branch in our model shown in Table I. Each layer details: input features, output features, kernel size, and stride. All other parameters are set to default. For our hand dataset, the number of joints is 21.

During our experiments, we found that training only using the ground truth as prior biased the model to expect perfect data. Conversely, training the model on its predictions only caused those inputs to be completely ignored because it never provided any useful data. Therefore, we found it beneficial to bootstrap our model with the ground truth priors but adopting a linear scheduling strategy to gradually introduce the model's own predictions. At each epoch, we select the model's prediction as a prior with a probability of $p = 1 - 0.10 * epoch$. By the 10th epoch, the model is training with all its predictions. We found this to be a good balance that slowly taught the model to use prior data even when imperfect.

Branch	Layer details
Atten. Mechanism	Conv2d(64 + num joints, 256, 3, 1)
	ReLU
	Conv2d(256, 256, 2, 2)
	ReLU
Fusing Module	ConvTranspose2d(256, num joints, 4, 2)
	Conv2d(2 × num joints, 256, 3, 1)
	ReLU
	Conv2d(256, 256, 2, 2)
	ReLU
	ConvTranspose2d(256, num joints, 4, 2)

TABLE I: Network architecture details on the branches in our model. Each layer shows the number of input features, output features, kernel size, and stride.

III. PERFORMANCE OF OBJECT DETECTOR ON DATASET

In our results, we showed scores using both a “perfect detection” and “object detection” system. A bottleneck in our system is the performance of the pre-trained hand object detector [?], which shows room for improvement on our data. Table II follows the detection evaluation format of MSCOCO [?]. The most notable issue is the low recall across all detection thresholds. The detector used was not trained on our data, which introduces many novel and difficult scenes. We show the number of detections filtered through for each detection threshold in the second column. AP computes the average precision at IoU thresholds 0.5 to 0.9 (in increments of 0.05). While AP50 and AP75 use only IoU thresholds 0.5 and 0.75, respectively. AR1 and AR10 measure the average recall on images with a maximum of 1 and 10 detections per image.

TABLE II: Object Detection Metrics of Hand Detections across detection thresholds

Det. Thresh	Num Det.	AP	AP50	AP75	AR1	AR10
0.9	49.9k	0.021	0.053	0.013	0.149	0.293
0.75	53.9k	0.022	0.056	0.013	0.153	0.311
0.5	57.6k	0.023	0.059	0.013	0.157	0.325
0.25	61.7k	0.024	0.061	0.014	0.159	0.335

IV. ADDED OPTICAL FLOW

We re-implemented part of the baseline [?], to include optical flow during tracking, although this has no impact on the output of the pose estimation model. We show these results in Table III.

Unexpectedly, adding optical flow to the tracking has a generally negative impact on the overall scores. We suspect that this is because the average size of our objects in relation

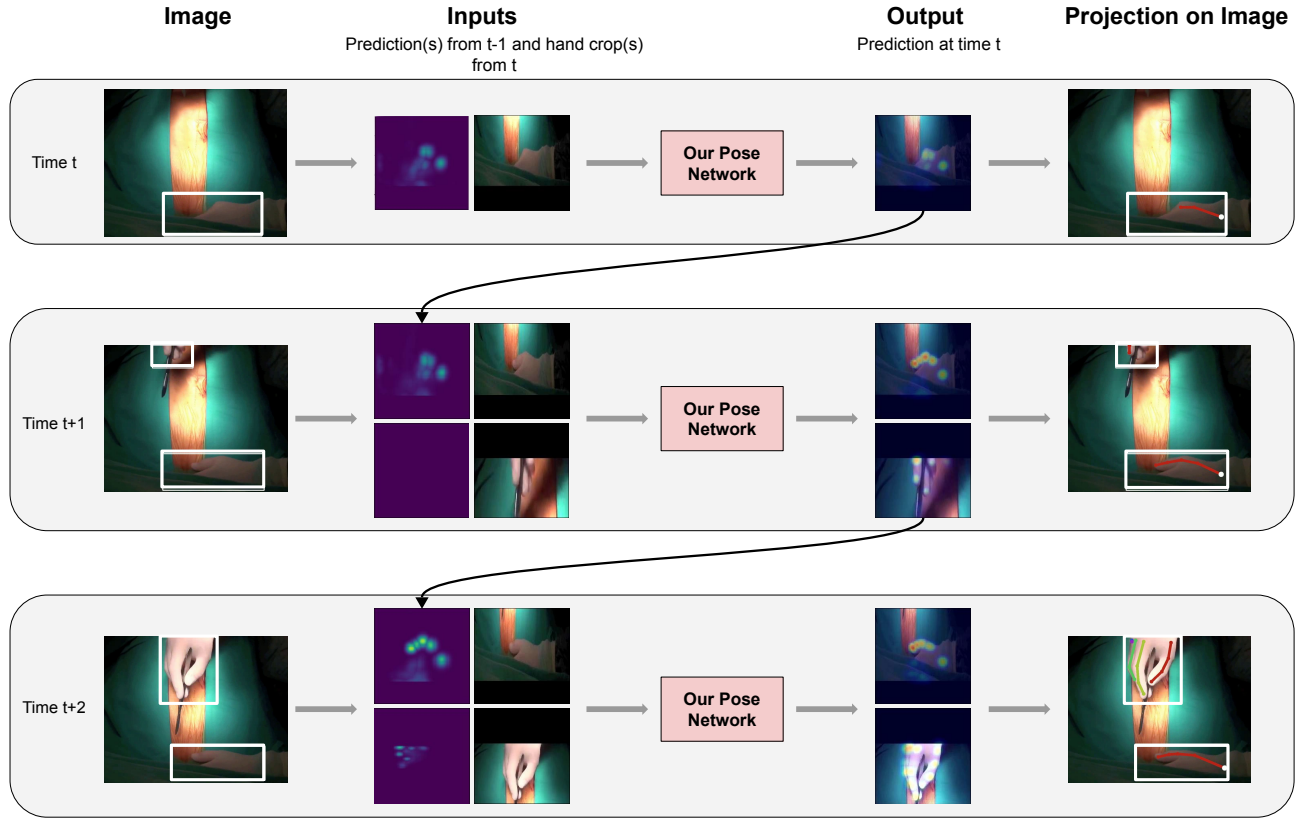


Fig. 1: A detailed overview of our model during evaluation on videos. Like training, newly introduced objects are accompanied with a blank, zero heatmap prior. We use two post-processing steps to filter out improbable priors when assigning matches. Each image crop is padded and centered on the detected hand.

to the image resolution. Our dataset consists of close-up views of hands in the surgical scene. The average size of each hand bounding box is 334^2px while the average area of our frames are 891^2px . We hypothesize that the small optical flow shifts of the detected boxes and poses, on average, is more likely to incorrectly adjust these positions.

TABLE III: MOTA performance between matching strategies, averaged across all folds. Each row is optimized for highest MOTA performance. Matching strategies share the same base model, so it is possible for them to share the same mAP score. Parenthesis show added optical flow.

Model	Matching Strategy	Perfect Det.		Object Det.	
		mAP	MOTA	mAP	MOTA
Baseline	IoU	53.59 (-0.93)	38.27 (-0.16)	48.15 (-0.71)	31.46 (-0.07)
	L2	52.65 (+0.0)	37.78 (-0.01)	47.44 (+0.0)	31.14 (-0.04)
	GCN	52.65 (+0.0)	36.78 (+0.0)	47.44 (-0.79)	30.03 (-0.28)
	GCN-Joint Visual	52.65 (+0.93)	36.64 (-0.1)	47.44 (+0.0)	30.17 (-0.12)
Our Model	IoU	56.66 (+0.0)	39.31 (-0.18)	50.04 (+0.0)	33.19 (-0.07)
	L2	56.66 (+0.0)	38.94 (-0.01)	50.04 (+0.0)	32.84 (-0.04)
	GCN	56.66 (+0.0)	38.22 (+0.04)	50.04 (-0.66)	32.24 (-0.25)
	GCN-Joint Visual	56.66 (+0.86)	38.25 (-0.06)	51.28 (-1.25)	32.39 (-0.09)